Ceramics-Silikáty 69 (2), 171-180 (2025)
www.ceramics-silikaty.cz doi: 10.13168/cs.2025.0003

OPTIMISATION OF THE PH AND LATEX VOLUME FOR EXPANDED SURFACE AREA OF HYDROXYAPATITE USING THE RESPONSE SURFACE METHODOLOGY

#AHMAD FADLI*, SRI HELIANTY*, DIMAS PRAMITA NUGRAHA**, FEBLIL HUDA***, NABILLA PUTRI ANDINI*, PUTRI ELVIRA*, AGUNG PRABOWO*

*Department of Chemical Engineering, Faculty of Engineering, Riau University, Pekanbaru, Riau, Indonesia
**Department of Pharmacology, Faculty of Medical, Riau University, Pekanbaru, Riau, Indonesia
***Department of Mechanical Engineering, Faculty of Engineering, Riau University, Pekanbaru, Riau, Indonesia

#E-mail: fadliunri@yahoo.com

Submitted November 6, 2024, accepted January 27, 2025

Keywords: Hydroxyapatite, Precipitation, Latex, Optimisation, Response Surface Methodology

Hydroxyapatite is widely utilised in biomedical applications, particularly in microcarriers and drug delivery, due to its stable and bioactive properties. This study focuses on optimising the pH and latex volume to enhance the surface area of hydroxyapatite synthesised via the precipitation technique, employing the Response Surface Methodology. The optimal response for hydroxyapatite was achieved at a pH of 10 and a latex volume of 0.75 mL, resulting in a specific surface area, pore size, and density of 38.86 $m^2 \cdot g^{-1}$, 45.84 nm, and 0.4 $cc \cdot g^{-1}$, respectively. The empirical model yielded R^2 values of 93.97 %, 88.06 %, and 96.93 % for each response variable, respectively. A desirability value of 0.915 indicates a highly acceptable optimisation level. The optimum conditions were found to be a pH of 10.0428 and a latex volume of 0.7632 mL, yielding values of 36.0217 $m^2 \cdot g^{-1}$, 41.929 nm, and 0.3919 $cc \cdot g^{-1}$, respectively. The crystallinity of the porous hydroxyapatite was determined to be 67.8 %, with an average crystal size of 315.9 nm, and the morphology exhibited a spherical shape with a Ca/P ratio of 1.69.

INTRODUCTION

Hydroxyapatite (HAp) is an apatite compound with the formula $Ca_{10}(PO_4)_6(OH)_2$ [1]. It is a stable inorganic chemical compound [2] known for its biocompatibility [3], non-inflammation [4], osteoconductivity [1], non-toxicity, and bioactivity [4]. Porous HAp has been widely used as a bone implant material due to its bioactive properties and its strong bonding to bone [5]. Additionally, porous HAp serves as an effective scaffold for tissue engineering. Its porous structure establishes a tight connection to bone, where the interlocking pores facilitate stronger fixation of the implant [1]. HAp with an open pore structure is ideal for promoting the proliferation of peripheral cells at the site of bone defects, as well as serving as a source of ions and stimuli for new bone formation [1].

Porous HAp is particularly noted for its high level of cell proliferation after cultivation, demonstrating excellent biocompatibility, high surface permeability, and specific surface area [2]. The pore structure in bioceramics typically exhibits porosity levels of up to 90 %, allowing for various applications across size ranges: macro (d > 50 nm), meso (50 nm > d > 2 nm), and micro (d < 2 nm) [1]. Porous HAp can be applied in medical fields, including the fixation of damaged bones and teeth [6], tissue engineering systems [7], drug delivery systems [8], implant composites [9], bone grafts [10], adsorbents [11], fertilisers [12], catalysts [13], and bone fillers [14]. HAp is essential for bone regeneration [15], as calcium (Ca) and phosphate (P) are its two major components, strengthening the mechanical properties of the organic matrix. Bone contains approximately 80 % to 90 % Ca and P [16]. HAp plays a critical role in bone regeneration and the formation of a strong bone structure [17]. HAp materials can be utilised in various forms, including porous, solid, granular ones, and as coatings [18]. It is primarily used in powder form, and its effectiveness depends on the powder's properties, such as a large surface area [19]. A large surface area with high porosity enhances both the quality and quantity of open pore structures in porous HAp [20].

Several methods can be used to achieve the synthesis of hydroxyapatite (HAp), including precipitation [1, 2, 21], emulsion [22], hydrothermal [23], solid-state [24], mechanochemical [25], sonochemical [26], co-precipitation [27], hydrolysis [28], and pyrolysis [29]. The precipitation method is straightforward, cost-effective, and scalable [30]. Pores in HAp can be created by adding a porogen, such as latex [27] or chitosan [2].

Additionally, pores in a scaffold can be formed using a template (e.g., banana midrib) along with a protein (e.g., egg yolk) and starch (e.g., sago flour) [31]. The use of latex can enhance porosity by up to 70 % with high efficiency. Latex can be easily removed using chemical solvents or by calcining at high temperatures (> 500 °C) [27].

The objective of this research is to define the optimum process parameters for porous HAp synthesis by varying the pH and latex volume. The pH significantly affects the surface area of HAp; an increase in pH can enhance this surface area [21]. Stable HAp synthesis occurs at a pH of 10, where phosphate compounds predominantly exist in the form of PO_4^{3-} [32]. The use of latex as a porogen for HAp porosity has been previously studied [27] in conjunction with the co-precipitation method. In this study, the pH and latex volume were manipulated as process variables using the precipitation method. A characterisation analysis was conducted using the Response Surface Methodology (RSM), a statistical and mathematical approach for optimising and modelling processes, as well as evaluating interactions between multiple variables. Optimal responses were generated using the desirability function across multiple empirical equations [1]. The optimum process conditions were assessed to produce a more effective porous HAp with the appropriate variables. Through this optimisation research, we aim to facilitate future studies by providing clear process variables for similar methods and raw materials. In this research, RSM employed Central Composite Design (CCD) to investigate the effects of the pH and latex volume on the surface area, pore size, and pore volume of porous HAp

EXPERIMENTAL

The materials used in this study were eggshell waste as a calcium precursor, di-ammonium hydrogen phosphate as another precursor (Merck, Indonesia), liquid latex as a porogen (Brataco Chemical, Indonesia), 65 % HNO_3 (Merck, Indonesia), a 25 % ammonium solution (Merck, Indonesia), and NH_4Cl (Merck, Indonesia) as a buffer solution.

Synthesis of calcium oxide (CaO)

Eggshell waste as a calcium precursor was prepared from washed, crushed, and milled eggshells, which were then sieved using a mesh size of 100. After sieving, the eggshells were calcined to obtain calcium oxide (CaO) using a furnace at 1000 °C for 5 hours. Following calcination, the CaO powder was characterised by Atomic Absorption Spectroscopy (AAS) (Varian SPECTRA 240) to determine the calcium content. The results of this characterisation were used to calculate the mass of CaO needed to prepare a calcium solution based on a predetermined concentration. Initially, hydroxyapatite (HAp) was synthesised using the chemical precipitation method by adding a $Ca(NO_3)_2$ solution.

Synthesis of porous hydroxyapatite

The synthesis process involved the controlled addition of $(NH_4)_2HPO_4$ to a buffered solution at pH 10, followed by the dropwise addition of liquid latex. The mixture was stirred at 300 rpm and 70 °C. After this initial heating phase, the solution was stirred continuously at room temperature for an additional 30 minutes. Following this, a milky suspension was formed after precipitation, which was then incubated at room temperature for 24 hours. The resulting precipitate was filtered using Whatman 42 filter paper and subsequently washed with Aqua Bidest distilled water to remove the acidic residue and by-products, specifically ammonium nitrate. The precipitate was dried in an oven at 110 °C for 5 hours and then calcined at 600 °C for 5 hours to obtain the porous HAp powder.

Characterisation of the porous HAp

The specific surface area, pore size, and pore volume of the synthesised HAp were characterised using the Brunauer-Emmett-Teller & Barrett-Joyner-Halenda (BET-BJH) analysis (Quantachrome NOVA 4200e Type STSA). An X-ray diffraction (XRD) analysis (Bruker AXS Type D8 Advance) was employed to identify the crystalline phases and provide information on the unit dimensions, including the crystal size and degree of crystallinity. The dimensions and morphological characteristics of the powders were examined using field emission scanning electron microscopy coupled with energy dispersive X-ray spectroscopy (FESEM-EDX, Thermo Scientific Quattro S).

Optimisation of the process conditions

In this study, a Central Composite Design (CCD) based on the Response Surface Methodology (RSM) was utilised for the experimental design, implemented via Design Expert 11 software. A total of 11 experimental runs were conducted, with desired variables set at ranges of ± 1 for the factorial points, 0 for the centre point, and ± α for the axial points, as detailed in Table 1. The parameters obtained from the optimisation process included a regression analysis, an analysis of variance

Table 1. The experimental design used the central composite design of RSM.

Process conditions	Unit	Coded variable levels				
		−α	−1	0	1	α
pH		8.58	9.00	10.00	11.00	11.41
Latex volume	mL	0.40	0.50	0.75	1.00	1.10

(ANOVA), empirical models, and both 2D and 3D plots. The process conditions of the pH and latex volume were optimised to achieve a desirability value close to 1, indicating that the optimisation results were suitable for the model employed.

RESULT AND DISCUSSION

BET-BJH analysis

A BET analysis was performed to determine the specific surface area, while a BJH analysis was used to ascertain the pore size and volume. The results of the BET-BJH analysis for each run are presented in Table 2. The synthesis of HAp was most stable at pH 10, as phosphate predominantly exists in the form of PO_4^{3-}. A decrease in the surface area was observed due to the presence of an excessive amount of porogen, which led to solution saturation. As shown in Table 2, the surface area decreased to 10.61 $m^2 \cdot g^{-1}$ and 21.68 $m^2 \cdot g^{-1}$ at a latex volume of 0.75 mL, with pH values of 8.58 and 11.41, respectively.

Table 2. Results of the BET-BJH analysis for each of the process variables.

Runs	pH	Latex vol. (mL)	Surface area ($m^2 \cdot g^{-1}$)	Pore size (nm)	Pore vol. ($cc \cdot g^{-1}$)
S1	10.00	0.75	35.27	45.84	0.40
S2	11.41	0.75	21.68	15.39	0.08
S3	10.00	1.10	20.96	25.44	0.12
S4	9.00	1.00	17.84	28.55	0.13
S5	10.00	0.40	27.57	25.02	0.17
S6	8.58	0.75	10.61	14.88	0.04
S7	10.00	0.75	38.86	40.82	0.40
S8	11.00	1.00	18.22	32.04	0.15
S9	11.00	0.50	20.95	12.95	0.06
S10	9.00	0.50	21.37	16.25	0.07
S11	10.00	0.75	34.10	38.60	0.37

The addition of latex at a volume of 0.75 mL demonstrated optimal process conditions for the synthesis of porous HAp. The introduction of the porogen (latex) resulted in the formation of a porous material, thereby increasing the surface area of HAp. At a low pH (< 10), a reduction in the surface area was noted, attributed to the decomposition of the HAp molecules into their constituent cations and anions. Conversely, at a high pH (> 10), the increase in hydroxide ions during synthesis negatively impacted the surface area, suggesting that the purity and stability of the synthesised HAp were compromised at elevated pH levels.

The results of the BJH analysis are illustrated in the nitrogen adsorption-desorption isotherm chart (Figure 1). The porous HAp particles exhibited physisorption isotherms of type IV, characterised by hysteresis loops of type H3. Such isotherms are indicative of porous materials with both micropore and mesopore characteristics. The presence of type H3 hysteresis loops suggests the formation of multilayers, with pore sizes classified as mesopores (2-50 nm).

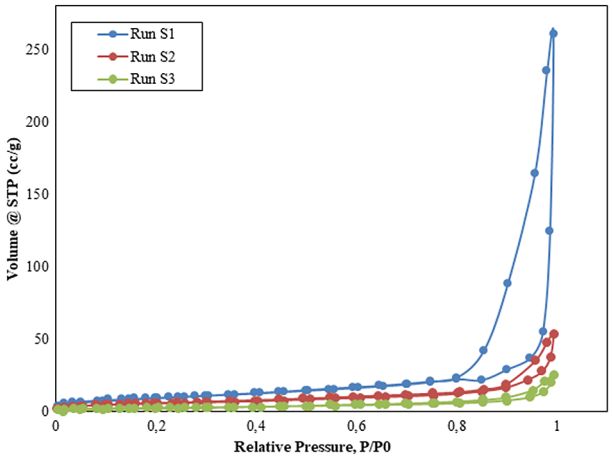

Figure 1. Nitrogen adsorption-desorption isotherm of the porous Hap.

Analysis of variance (ANOVA)

For the analysis of variance (ANOVA) conducted using the statistical software Design Expert 11, quadratic models were selected for all the interactions of the responses. Based on the fit summary results (Table 3), the quadratic model was recommended as it met the criteria with a p-value of less than 0.05, indicating an error rate below 5 %. In contrast, the aliased model was not considered suitable [38]. The ANOVA results for each response (Table 4) demonstrate whether the selected polynomial equations significantly impacted the experimental design. A p-value less than 0.05 ($p < 0.05$) indicates that the models have a confidence level of

Table 3. Fit summary for each response.

Fit summary	Quadratic			Cubic		
	Y_1	Y_2	Y_3	Y_1	Y_2	Y_3
Sequential p-value	0.0011	0.0065	0.0003	0.1573	0.1187	0.0258
Lack of fit p-value	0.3817	0.2520	0.1184	0.7575	0.4788	0.7211
Adjusted R^2	0.8793	0.7611	0.9266	0.9414	0.9038	0.9893
Predicted R^2	0.6513	0.2529	0.7533	0.8966	0.4511	0.9774
	Suggested			*Aliased*		

Table 4. ANOVA for each response.

Source	F-value			p-value			
	Y_1	Y_2	Y_3	Y_1	Y_2	Y_3	
Model	15.5700	7.3700	26.240	0.0045	0.0234	0.0013	Significant
A-pH	3.4100	0.0033	0.4558	0.1239	0.9563	0.5296	
B-Latex volume	3.4100	4.0900	0.4916	0.1241	0.0991	0.5145	
AB	0.0197	0.3686	0.1239	0.8940	0.5703	0.7392	
A^2	64.4600	29.320	106.5700	0.0005	0.0029	0.0001	
B^2	23.1100	10.690	58.8900	0.0049	0.0222	0.0006	
Residual							
Lack of fit	1.7600	3.120	7.6000	0.3817	0.2520	0.1184	Not significant

95 %. If insignificant variables (A^2 and B^2) are identified within a significant model, they are retained since their exclusion does not affect the model's performance [39]. Insignificance in the lack of fit suggests that the models adequately fit the experimental design, while the significance in the lack of fit indicates a poor model fit [38].

The standard deviation serves as a measure of the predicted values, which should closely approximate the actual values; a decrease in standard deviation signifies greater predictive accuracy. The coefficient of variation (CV %) measures relative variability, expressed as the ratio of the standard deviation to the mean, represented as a percentage. A decrease in CV% indicates that the predicted data align more closely with the actual experimental data [38].

The model validation was assessed through the fit statistics of each response (Table 5). The R^2 values, which should be close to 1, were significantly high, suggesting that the models are highly reliable. A decrease in the R^2 value indicates a weaker relationship between the variables and the responses. In this study, the R^2 values for surface area, pore size, and pore volume were 0.9397, 0.8806, and 0.9633, respectively, demonstrating strong relationships between the variables and the responses. Adequate accuracy is indicated by the experimental signal-to-noise ratio, which compares the range of predicted values at the design points to an average prediction error exceeding 4 [38].

Table 5. Fit statistics for each response.

Fit statistic	Surface area (Y_1)	Pore aize (Y_2)	Pore volume (Y_3)
Standard deviation	3.00	5.59	0.0383
Mean	24.31	26.89	0.1805
C.V. %	12.32	20.80	21.25
R^2	0.9397	0.8806	0.9633
Adjusted R^2	0.8793	0.7611	0.9266
Predicted R^2	0.6513	0.2529	0.7533
Adequate precision	10.3998	6.3001	12.2209

Analysis of regression

The regression analysis encompasses a set of statistical procedures used to study the relationships between a dependent variable and its predicted values. Table 6 presents the coefficients of the coded equation assigned to each level of the variables (-1, 0, and +1), which indicate the directional relationships with the responses. These coefficients are employed to assess the effect of the variables on the factor coefficients, while the actual equation is utilised to predict the responses for each factor. However, this equation cannot determine the effect of each factor individually, as the selected coefficients may fall outside the range defined by the Central Composite Design (CCD) [38]. The independent variables for functions A and B are represented in Equations (1), (2), and (3).

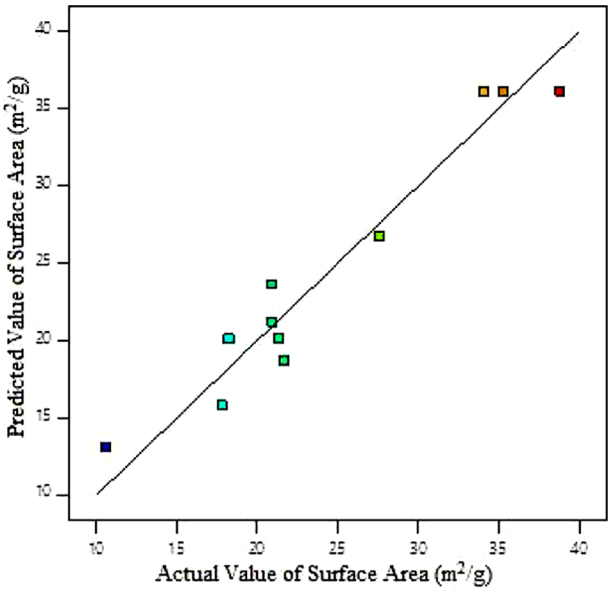

a)

Figure 2. Actual versus predicted plot of the responses: a) surface area. *(Continue on next page)*

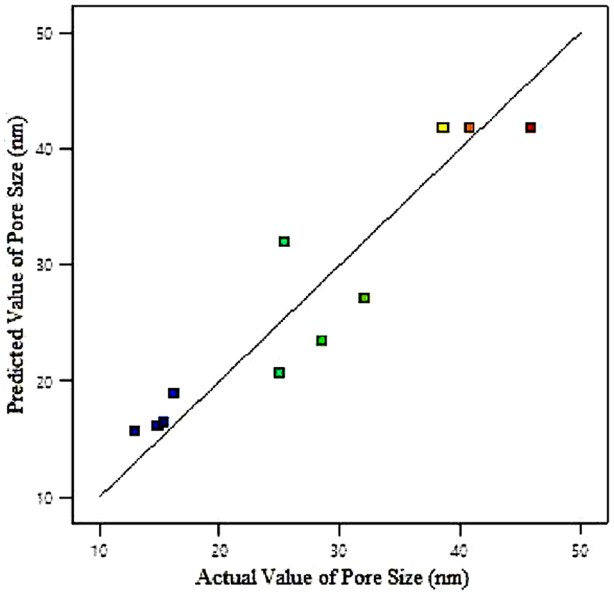

b)

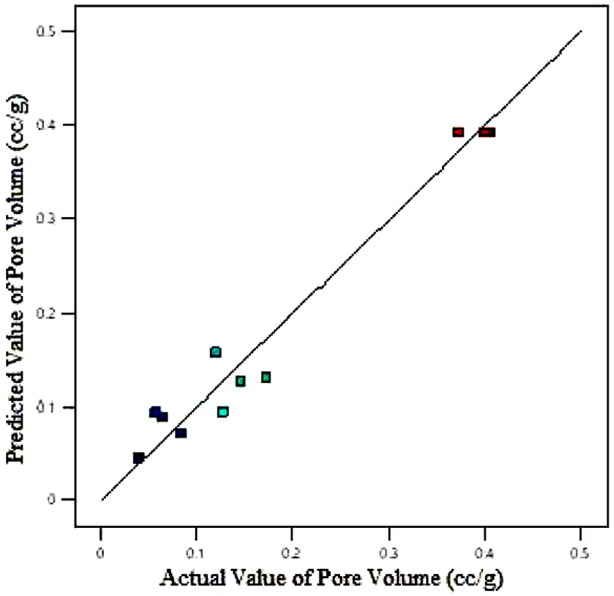

c)

Figure 2. Actual versus predicted plot of the responses: b) pore size, and c) pore volume.

A second-order polynomial equation was employed to ascertain the response values Y_1, Y_2, and Y_3 as independent variables. Notably, the negative coefficients for A^2 and B^2 indicated a maximum quadratic pattern. The residual versus predicted plots for surface area (Figure 2a), pore size (Figure 2b), and pore volume (Figure 2c) illustrate the distribution of actual versus predicted values. The surface area and pore volume responses closely align with the linear regression line, while the pore size response is somewhat more distant. A close alignment of predicted and actual values to the linear line suggests that the selected models accurately describe the real conditions of the optimisation process. The closer the distribution values are to the linear line, the better the model selection, as supported by an R^2 value approaching 1. Therefore, this research demonstrates high precision and accuracy in the fitted data.

$$Y_1 = 36.08 + 1.96A - 1.96B + 0.21AB - -10.12A^2 - 6.06B \quad (1)$$

$$Y_2 = 41.75 + 0.1139A + 4B + 1.7AB - - 12.74A^2 - 7.7B^2 \quad (2)$$

$$Y_3 = 0.3917 + 0.0092A + 0.0095B + + 0.0067AB - 0.1666A^2 - 0.1238B^2 \quad (3)$$

Table 6. Coded equation and actual equation for each equation.

Equation	Surface area (Y_1)	Pore aize (Y_2)	Pore volume (Y_3)
Coded equation			
Intercept	+36.08	+41.75	+0.3917
A	+1.96	+0.1139	+0.0092
B	–1.96	+4.00	+0.0095
AB	+0.2100	+1.70	+0.0067
A^2	-10.12	–12.74	–0.1666
B^2	-6.06	–7.70	–0.1238
Actual equation			
Intercept	–1037.95536	–1264.00513	–17.29872
pH	+203.74358	+249.87974	+3.32057
Latex volume	+129.23602	+132.78198	+2.74002
pH * latex volume	+0.840000	+6.79000	+0.027000
pH^2	–10.12083	–12.74292	–0.166583
Latex volume^2	–96.97333	–123.12667	–1.98133

Contour plot (2D plot) and response surface plot (3D)

The interactions between the independent variables (pH and latex volume) and each response are illustrated in the contour and response surface plots (Figure 3). The optimum response values on the contour plot are indicated by the presence of nodes. Each response's surface plot reflects the optimum point, forming a curve that peaks at the centre, typically referred to as strictly concave. The highest responses observed were a surface area of 38.86 $m^2 \cdot g^{-1}$ (at S7), a pore size of 45 nm (at S1), and a pore volume of 0.404 $cc \cdot g^{-1}$ (at S1 and S7), achieved under the process conditions of pH 10 and a latex volume of 0.75 mL. From the 2D and 3D visualisations, it is evident that the pore volume exhibits the most significant effect among the responses and process variables.

Optimisation of the process condition and model validation

The optimisation of the process conditions was performed to enhance multiple output responses using the desirability function. In this context, the terms for the target (T), upper (U), and lower (L) limits were

defined, with each response aimed at maximising the set goals. The overall desirability value achieved was 0.915, corresponding to optimum process conditions of pH 10.0428 (Figure 4a) and a latex volume of 0.7632 mL (Figure 4b). The optimum responses obtained were a surface area of 36.0217 $m^2 \cdot g^{-1}$ (Figure 4c), a pore size of 41.929 nm (Figure 4d), and a pore volume of 0.3919 $cc \cdot g^{-1}$ (Figure 4e).

The desirability method is employed to define and control the optimal conditions necessary for minimising, maximising, or achieving nominal values for the specifications, thereby enabling the simultaneous optimisation of multiple responses. As presented in Table 7, the mathematical models for each Equation (1), (2), and (3) were validated by setting each variable to zero and using only the coefficient b_0 as the middle level for each factor.

Table 7. Validation of the mathematical models.

Factor level		Prediction value		
pH	Latex vol. (mL)	Surface area ($m^2 \cdot g^{-1}$)	Pore size (nm)	Pore vol. ($cc \cdot g^{-1}$)
0	0	36.08	41.75	0.3917

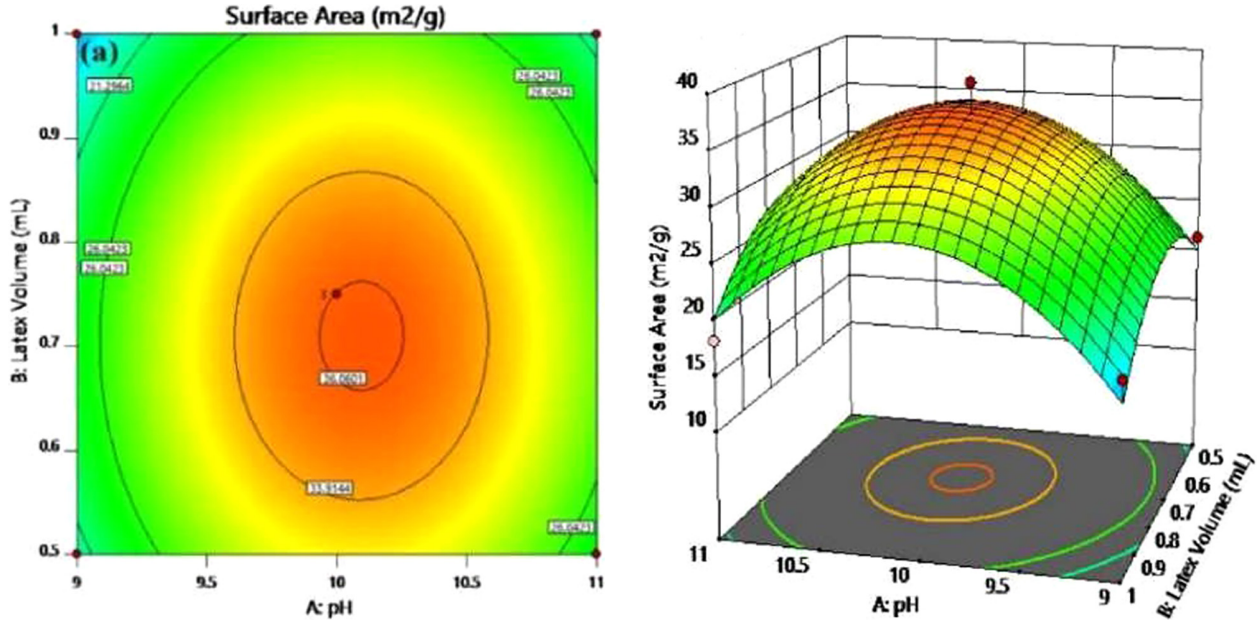

a)

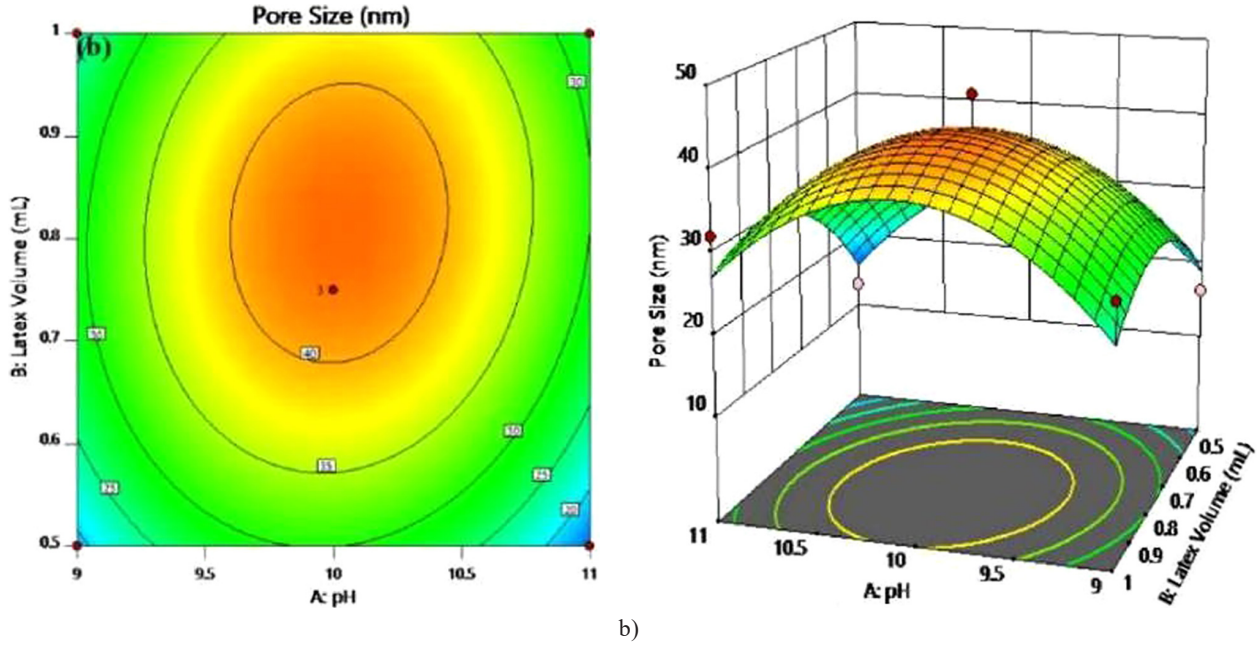

b)

Figure 3. Contour plot and the surface plot responses for the: a) surface area, b) pore size. *(Continue on next page)*

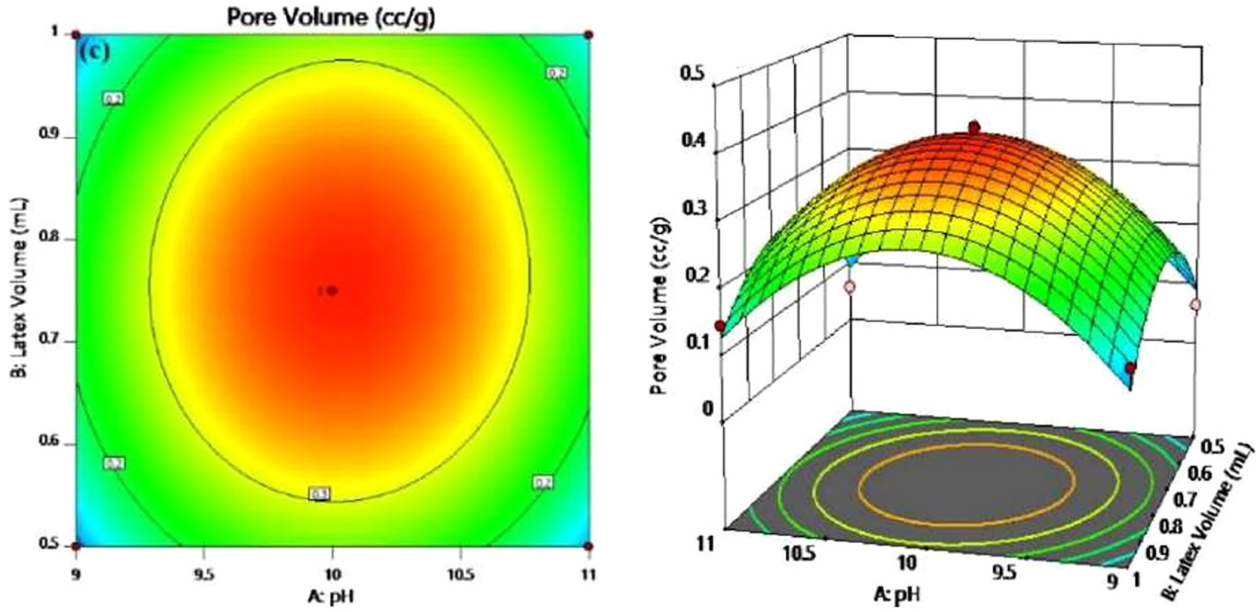

c)

Figure 3. Contour plot and the surface plot responses for the: c) pore volume.

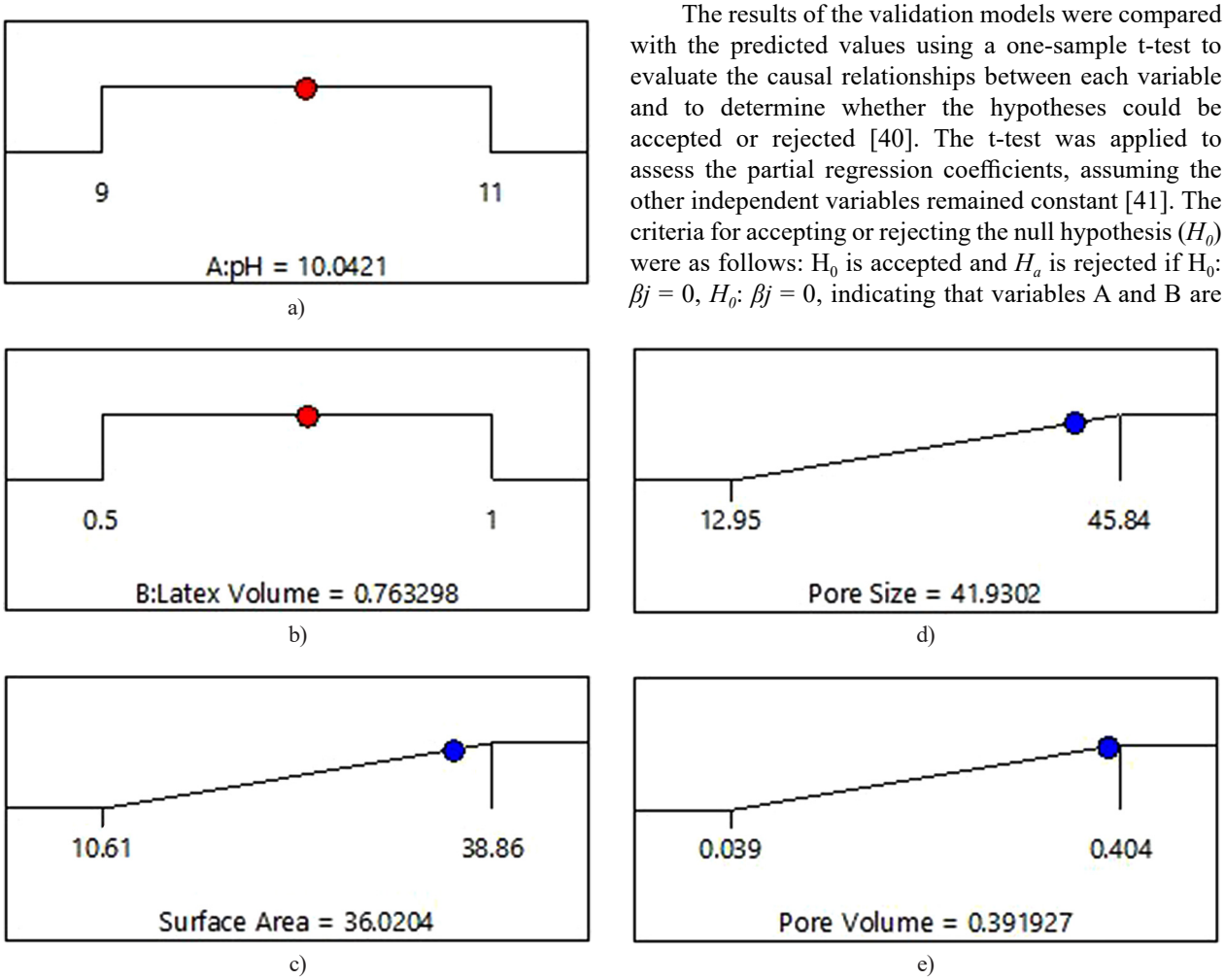

The results of the validation models were compared with the predicted values using a one-sample t-test to evaluate the causal relationships between each variable and to determine whether the hypotheses could be accepted or rejected [40]. The t-test was applied to assess the partial regression coefficients, assuming the other independent variables remained constant [41]. The criteria for accepting or rejecting the null hypothesis (H_0) were as follows: H_0 is accepted and H_a is rejected if H_0: $\beta j = 0$, H_0: $\beta j = 0$, indicating that variables A and B are

Figure 4. The results of the optimisation of the: a) pH, b) latex volume, c) surface area, d) pore size, and e) pore volume (desirability = 0.915; solution 1 out of 1).

insignificant to Y; conversely, H_0 is rejected and H_a is accepted if H_0: $\beta j = 0$, indicating that variables A and B are significant to Y. The next step involved calculating t-values and comparing them to critical t-values based on each response. The calculated t-values for surface area response, pore size, and pore volume were 11.842, 8.147, and 15.370, respectively, with a critical t-value of 2.228. Thus, since the calculated t-values exceeded the critical t-value, this indicates a significant effect.

X-Ray diffraction (XRD) analysis

X-ray diffraction (XRD) is a technique utilised to analyse the crystal structure, chemical composition, and physical properties of materials. Crystalline materials are examined using XRD to reveal specific diffraction peaks, which can also help identify any unknown compounds in the samples [36, 42]. As illustrated in Figure 5, several peaks correspond to the characteristic XRD pattern for hydroxyapatite, as referenced in JCPDS Diffraction Pattern 9-432, with specific 2θ diffraction angles. The sample with the highest surface area (S7) exhibited prominent peaks at 2θ angles of 25.824° and 31.064°, corresponding to a crystallinity of 67.8 %. This indicates a high degree of crystallinity, as evidenced by the narrow and sharp diffraction peaks.

The crystal sizes of hydroxyapatite were determined to be 308.1 nm and 315.9 nm. Additionally, two compounds were identified: hydroxyapatite and sodium calcium phosphate. The presence of sodium ions (Na^+) in the hydroxyapatite was attributed to the sodium content in the materials used, particularly from the eggshells and latex, which contained 0.152 % and 0.2–0.3 % sodium, respectively [37, 43].

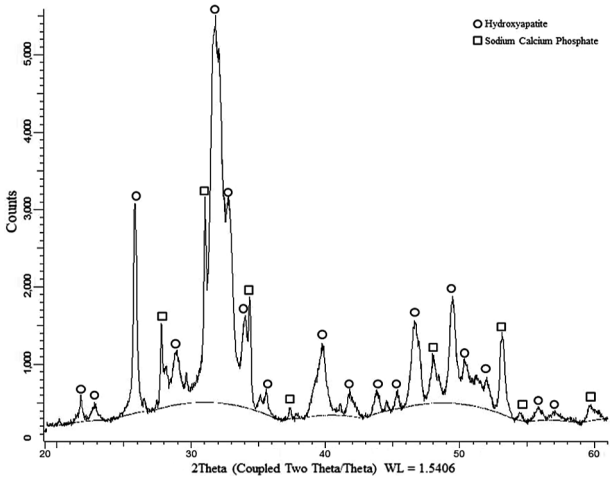

Figure 5. XRD pattern of the synthesised porous HAp (S7).

Particle morphology analysis

Porous hydroxyapatite (HAp) was characterised to determine the particle morphology using a field emission scanning electron microscopy (FESEM) analysis, complemented by energy-dispersive X-ray spectroscopy (EDX) to identify the constituent elements of the materials. Figure 6a presents the results of the FESEM characterisation at a magnification of 200,000×, while Figure 6b illustrates the EDX analysis. The particle morphology of HAp, as shown in Figure 6a, displays voids resulting from the use of latex as the porogen, which were eliminated during the calcination process at 600 °C. The calcination at 300 °C caused the latex to melt, disappearing above 500 °C, which contributed to the formation of pores in the HAp particles [33-35]. The morphology of HAp was characterised by agglomerations of irregularly spherical particles, with sizes less than 80 nm.

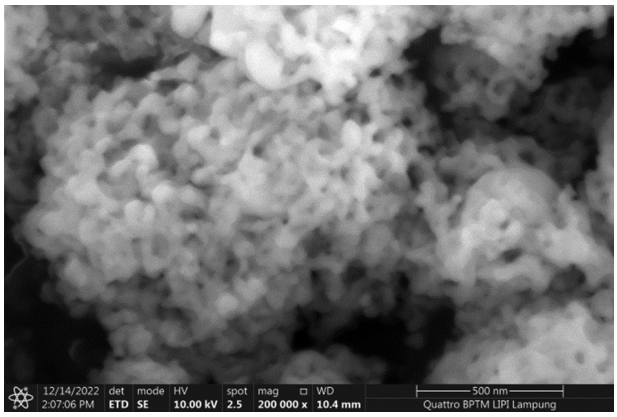

a)

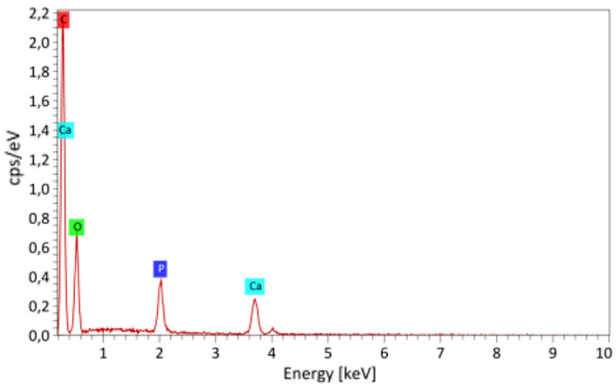

b)

Figure 6. Particle morphology analysis of the porous HAp (S7): a) FESEM b) EDX.

The calcium (Ca) and phosphorus (P) contents were analysed using EDX, revealing values of 4.91 % and 2.89 %, respectively, which resulted in a Ca/P ratio of 1.69. This ratio exceeds the stoichiometric Ca/P ratio of 1.67. The range of stoichiometric HAp is typically between 1.62 and 1.71 [44], indicating that the Ca/P ratio observed in this study falls within this acceptable range. The increase in the Ca/P ratio may be attributed to the presence of impurities, such as calcium oxide (CaO), as well as elevated calcium and oxygen contents detected during the EDX analysis.

CONCLUSION

The synthesis of porous hydroxyapatite (HAp) using latex as a porogen was successfully achieved through the precipitation method. The analysis revealed a surface area ranging from 10.61 to 38.86 $m^2 \cdot g^{-1}$, a pore size of 12.95 to 45.84 nm, and a pore volume of 0.04 to 0.4 $cc \cdot g^{-1}$. The crystallinity of the synthesised HAp was determined to be 67.8 %, with the largest crystal size measuring 315.9 nm. The morphology of HAp exhibited a spherical shape, accompanied by a calcium-to-phosphorus (Ca/P) ratio of 1.69. The significantly increased pore volume was influenced by both the pH and latex volume. The optimum process conditions were identified at a pH of 10.0428 and a latex volume of 0.7632 mL, resulting in optimal responses of the surface area (36.0217 $m^2 \cdot g^{-1}$), pore size (41.929 nm), and pore volume (0.3919 $cc \cdot g^{-1}$).

REFERENCES

1. Fadli A., Komalasari., Huda F., Ardi T., Habib I. (2022): Optimization of process condition on fabrication of porous hydroxyapatite bodies using banana midrib as template by response surface methodology. *Journal of Natural Fibers*, *19*(9), 3378-3393. DOI: 10.1080/15440478.2020.1848698.
2. Absalan F., Sadjadi M. S., Farhadyar N., Sadr M. H. (2020): Synthesis of mesoporous hydroxyapatite with controlled pore size using the chitosan as an organic modifier: investigating the effect of the weight ratio and pH value of chitosan on the structural and morphological properties. *Journal of Inorganic and Organometallic Polymers and Materials*, *30*(9), 3562-3573. DOI: 10.1007/s10904-020-01623-5.
3. Fadli A., Widiyanti P., Noviana D., Prabowo A., Mulyadi A., Deska (2022): Porous hydroxyapatite scaffold produced using Musa paradisiaca template and its in vitro bioactivity. *Journal of the Australian Ceramic Society*, 1-10. DOI: 10.1007/s41779-021-00677-z
4. Hapuhinna H. K. G. K. D. K., Gunaratne R. D., Pitawala H. M. J. C. (2019): A composite developed from a methyl methacrylate and embedded eppawala hydroxyapatite for orthopedics. DOI: 10.4236/msce.2019.75002.
5. Fadli A., Prabowo A., Komalasari K., Putra A. M., Yuza, B. (2024): Utilizations of various of starches for 3D design of femur bone replica manufacture. *F1000Research*, *13*, 383.. DOI: 10.12688/f1000research.128024.1.
6. Furukawa T., Matsusue Y., Yasunaga T., Nakagawa Y., Okada Y., Shikinami Y., Nakamura T. (2000): Histomorphometric study on high-strength hydroxyapatite/poly (L-lactide) composite rods for internal fixation of bone fractures. *Journal of Biomedical Materials Research: An Official Journal of The Society for Biomaterials, The Japanese Society for Biomaterials, and The Australian Society for Biomaterials and the Korean Society for Biomaterials*, *50*(3), 410-419. DOI: 10.1002/(SICI)1097-4636(20000605)50:3.
7. Seol Y. J., Kim J. Y., Park E. K., Kim S. Y., Cho D. W. (2009): Fabrication of a hydroxyapatite scaffold for bone tissue regeneration using microstereolithography and molding technology. *Microelectronic Engineering*, *86*(4-6), 1443-1446. DOI: 10.1016/j.mee.2009.01.053.
8. Fadli A., Amri A., Iwantono I., Adnan A., Sunarno S., Sukoco S., Mayangsari M. (2020): The oriented attachment model applied on crystal growth of hydrothermal derived magnetite nanoparticles. *Indonesian Journal of Chemistry*, *20*(2), 379-385. DOI: 10.22146/ijc.42917.
9. Fadli A., Prabowo A., Utama Panca setia., Aziz Y., Heltina D. (2023): Significance of the Pcl concentration on the electrochemical and mechanical performance of a Pcl/Ha coating on SS 316L. *Ceramics – Silikáty*, *67*(4), 551-561. DOI: 10.13168/cs.2023.0054
10. Dewi A. H., Ana, I. D. (2018): The use of hydroxyapatite bone substitute grafting for alveolar ridge preservation, sinus augmentation, and periodontal bone defect: A systematic review. *Heliyon*, *4*(10): DOI: 10.1016/j.heliyon.2018.e00884.
11. Nayak A., Bhushan B. (2021): Hydroxyapatite as an advanced adsorbent for removal of heavy metal ions from water: Focus on its applications and limitations. *Materials Today: Proceedings*, *46*, 11029-11034. DOI: 10.1016/j.matpr.2021.02.149.
12. Xiong L., Wang P., Hunter M. N., Kopittke P. M. (2018): Bioavailability and movement of hydroxyapatite nanoparticles (HA-NPs) applied as a phosphorus fertiliser in soils. *Environmental Science: Nano*, *5*(12), 2888-2898. DOI: 10.1039/c8en00751a.
13. Usami K., Okamoto A. (2017): Hydroxyapatite: catalyst for a one-pot pentose formation. *Organic & Biomolecular Chemistry*, *15*(42), 8888-8893. DOI: 10.1039/c7ob02051a.
14. Kattimani V. S., Kondaka S., Lingamaneni K. P. (2016): Hydroxyapatite – Past, present, and future in bone regeneration. *Bone and Tissue Regeneration Insights*, *7*, BTRI-S36138. DOI: 10.4137/BTRi.s36138.
15. da Silva M.P., Moura F N., da Rocha D.N., Gobbo L.A., Costa A.M., Louro L.H.L. (2014): Zinc-modified hydroxyapatite coatings obtained from parascholzite alkali conversion. *Surface and Coatings Technology*, *249*, 109-117. DOI: 10.1016/j.surfcoat.2014.03.052
16. Bonjour, J. P. (2011): Calcium and phosphate: a duet of ions playing for bone health. *Journal of the American College of Nutrition*, *30*(sup5), 438S-448S. DOI: 10.3390/ma13122736.
17. Deo K. A., Lokhande G., Gaharwar A. K. (2019): Nanostructured hydrogels for tissue engineering and regenerative medicine. *Encyclopedia of tissue engineering and regenerative medicine*, *1*, 3.. DOI: 10.1016/B978-0-12-801238-3.11114-6.
18. Yenti S. R., Fadli A., Amri A., Novandri D., Setiawan F., Hasibuan J., Prabowo A., Herjan V. G. T. (2023): Synthesis of hydroxyapatite powder using natural latex particles as pore-creating agent. *Materials Today: Proceedings*, *87*, 278-283. DOI: 10.1016/j.matpr.2023.03.282.
19. Uota M., Arakawa H., Kitamura N., Yoshimura T., Tanaka J., Kijima, T. (2005): Synthesis of high surface area hydroxyapatite nanoparticles by mixed surfactant-mediated approach. *Langmuir*, *21*(10), 4724-4728. DOI: 10.1021/la050029m.
20. Yenti S. R., Fadli A., Hermawan D. A., Prabowo A., Yuza, B. (2024, July): The empirical model to predict surface area of porous hydroxyapatite particles prepared using latex as a pore-forming template. In *AIP Conference Proceedings* (Vol. 3027, No. 1): AIP Publishing. DOI: 10.1063/5.0206259

21. Lee I. H., Lee J. A., Lee J. H., Heo Y. W., Kim, J. J. (2020): Effects of pH and reaction temperature on hydroxyapatite powders synthesized by precipitation. *Journal of the Korean Ceramic Society*, *57*(1), 56-64. DOI: 10.1007/s43207-019-00004-0.
22. Kamieniak J., Kelly P. J., Banks C. E., Doyle A. M. (2018): Mechanical, pH and thermal stability of mesoporous hydroxyapatite. *Journal of Inorganic and Organometallic Polymers and Materials*, *28*, 84-91. DOI: 10.1007/s10904-017-0652-3
23. Azis Y., Jamarun N., Arief S., Nur, H. (2015): Facile synthesis of hydroxyapatite particles from cockle shells (Anadaragranosa) by hydrothermal method. *Oriental journal of chemistry*, *31*(2), 1099-1105. DOI: 10.13005/ojc/310261
24. Javadinejad H.R., Ebrahimi-Kahrizsangi R. (2021): Thermal and kinetic study of hydroxyapatite formation by solid-state reaction. *International Journal of Chemical Kinetics*, *53*(5), 583-595. DOI: 10.1002/kin.21467
25. Fadli A., Yenti S. R., Rasyidin R., Sari M. (2019, May): The effect of time and number of balls on shaker milling process in hydroxyapatite powder synthesis. In *IOP Conference Series: Materials Science and Engineering* (Vol. 532, No. 1, p. 012012): IOP Publishing. DOI: 10.1088/1757-899X/532/1/012012.
26. Utara S., Klinkaewnarong J. (2015): Sonochemical synthesis of nano-hydroxyapatite using natural rubber latex as a templating agent. *Ceramics International*, *41*(10), 14860-14867. DOI: 10.1016/j.ceramint.2015.08.018.
27. Weble G.D., Rordrigues W.C., Silva A.E.S., Silva A.O.S., Fonseca E.J.S., et al. (2018): Use of micrometric latex beads to improve the porosity of hydroxyapatite obtained by chemical coprecipitation method. *Applied Surface Science*, *436*, 141-151.141–151. DOI: 10.1016/j.apsusc.2017.11.218.
28. Shih W.J., Wang M.C., Hon M.H. (2005): Morphology and crystallinity of the nanosized hydroxyapatite synthesized by hydrolysis using cetyltrimethylammonium bromide (CTAB) as a surfactant. *Journal of Crystal Growth*, *275*(1-2), e2339-e2344. DOI: 10.1016/j.jcrysgro.2004.11.330.
29. Cho J.S., Rhee S.H. (2013): Formation mechanism of nanosized hydroxyapatite powders through spray pyrolysis of a calcium phosphate solution containing polyethylene glycol. *Journal of the European Ceramic Society*, *33*(2), 233-241. DOI: 10.1016/j.jeurceramsoc.2012.08.029.
30. Barui S., Hadagalli K., Mukherjee S., Roy S., Bhattacharjee D., Basu B. (2022): Pilot-scale manufacturing of phase-pure and highly crystalline hydroxyapatite: Lessons learned and process protocols. *International Journal of Applied Ceramic Technology*, *19*(2), 762-772. DOI: 10.1111/ijac.13953
31. Sopyan I., Fadli A., Mel M. (2012): Porous alumina – hydroxyapatite composites through protein foaming – consolidation method. *Journal of the mechanical behavior of biomedical materials*, *8*, 86-98. DOI: 10.1016/.j.jmbbm.2011.10.012.
32. Mishra V. K., Bhattacharjee B. N., Kumar D., Rai S. B., Parkash O. (2016): Effect of a chelating agent at different pH on the spectroscopic and structural properties of microwave derived hydroxyapatite nanoparticles: a bone mimetic material. *New Journal of Chemistry*, *40*(6), 5432-5441. DOI: 10.1039/C5NJ03322E.
33. Li X., Gao Z., Fang S., Ren C., Yang K., Wang F. (2019): Fractal characterization of nanopore structure in shale, tight sandstone and mudstone from the Ordos Basin of China using nitrogen adsorption. *Energies*, *12*(4), 583. DOI: 10.1039/c8en00751a.
34. Cholas R., Padmanabhan S.K., Gervaso F., Udayan G., Monaco G., Sannino A., Licciulli A. (2016): Scaffolds for bone regeneration made of hydroxyapatite microspheres in a collagen matrix. *Materials Science and Engineering: C*, *63*, 499-505. DOI: 10.1016/j.msec.2016.03.022.
35. Bakhtiari L., Javadpour J., Rezaie H.R., Erfan M., Shokrgozar M.A. (2015): The effect of swelling agent on the pore characteristics of mesoporous hydroxyapatite nanoparticles. *Progress in Natural Science: Materials International*, *25*(3), 185-190. DOI: 10.1088/1741-6596/1372/1/012018.
36. Epp J. (2016): X-ray diffraction (XRD) techniques for materials characterization. In *Materials characterization using nondestructive evaluation (NDE) methods* (pp. 81-124): Woodhead Publishing.
37. Despetis F., Bengourna N., Lartigue B., Spagnol S., Olivi-Tran, N. (2012): Three-dimensional reconstruction of aerogels from TEM images. *Journal of non-crystalline solids*, *358*(9), 1180-1184. DOI: 10.1016/j.jnoncrysol.2012.02.018.
38. Akram W., Garud N. (2021): Design expert as a statistical tool for optimization of 5-ASA-loaded biopolymer-based nanoparticles using Box Behnken factorial design. *Future Journal of Pharmaceutical Sciences*, *7*, 1-17. DOI: 10.1186/s43094-021-00299-z.
39. Fern H.W., Salimi, M. N. (2021): Hydroxyapatite nanoparticles produced by direct precipitation method: Optimization and characterization studies. In *AIP Conference Proceedings* (Vol. 2339, No. 1): AIP Publishing. DOI: 10.1063/5.0044252.
40. Pyrczak F., Oh D.M. (2018): *Making sense of statistics: A conceptual overview*. Routledge.
41. Lan W., Zhong P.S., Li R., Wang H., Tsai C.L. (2016): Testing a single regression coefficient in high dimensional linear models. *Journal of Econometrics*, *195*(1), 154-168. DOI: 10.1016/j.jeconom.2016.05.016.
42. Fadli A., Yenti S.R., Huda F., Prabowo A., Marbun U.N. (2021): Empirical model to predict the hydroxyapatite thickness on the surface of 316l stainless steel by the dip coating method. *Ceramics – Silikáty*, *65*(4), 386-394. DOI: 10.13168/cs.2021.0041.
43. Dermawan S.K., Ismail Z.M.M., Jaffri M.Z., Abdullah H.Z. (2022): Effect of the calcination temperature on the properties of hydroxyapatite from black tilapia fish bone. In *Journal of Physics: Conference Series* (Vol. 2169, No. 1, p. 012034): IOP Publishing. DOI: 10.1088/1742-6596/2169/1/012034.
44. Pu'ad N.M., Alipal J., Abdullah H.Z., Idris M.I., Lee T.C. (2021): Synthesis of eggshell derived hydroxyapatite via chemical precipitation and calcination method. *Materials Today: Proceedings*, *42*, 172-177. DOI: 10.1016/k.matpr.2020.11.276.